Appendix A Evolution of the kink instability

Figure A1 shows the initial kink instability before, during, and after the flux rope disruption. Initially ($t = 0$ s), the cold and dense material is trapped inside the twisted magnetic strand (Fig. A1, upper panel). During the onset of the kink instability ($t \sim 100$ s), a helical perturbation develops and heats up the external shell of the flux tube (Fig. A1, mid panel). At $t \sim 200$ s, the magnetic field structure and the material inside have fragmented (Fig. A1, lower panel). During the linear phase of the kink instability, the magnetic energy drops and releases about 10^{30} erg into kinetic and internal energy (Fig. A2, left panel). The evolution is consistent with previous results [34] that predict an exponential increase of the kinetic energy (with a secondary bump later on) and a smoother evolution of the internal energy. In addition, the current density increases exponentially (Fig. A2, upper right panel), together with the temperature, as the helical current sheet develops [34]. There is a short temporal delay between the current density peak and the temperature peak. Afterwards, the trajectory becomes more irregular because the magnetic field has fragmented into many current sheets, releasing localised, impulsive heating. After a short delay from the onset of the instability, also the intensities through the SDO/AIA, SolO/EUI, and IRIS channels follow an exponential trend, growing steeply by one order of magnitude in a few seconds (Fig. A2, bottom panel). After the onset of the kink instability, the filament plasma fragments into multiple dense clumps, transitioning from a monolithic structure to a highly inhomogeneous medium with a morphology akin to coronal rain [61], as the clumps subsequently fall along the magnetic flux tube under gravity.

Appendix B Reconnection dynamics

The reconnection event that leads to the nanojet acceleration takes place around $z \sim 0$ Mm. This is emphasized in Fig. B3 by the orange and magenta field lines that cross each other around the center of the box at time $t = 235$ s (upper panel). The nanojet originates from a region of dense plasma at $z \sim 7$ Mm that is crossed by the orange line only. After ~ 14 s (lower panel), the field lines have switched the magnetic connectivity at the (positive-z) footpoint, and the released magnetic tension has pushed them away from the current sheet. The lower panel B3 shows the orange line dragging part of the cold plasma, resulting in the detected nanojet (green volume).

Appendix C Analysis of synthetic observations

To show in detail the respective contributions of cold and hot plasma to the intensity maps in Fig. 3, we plot in Fig. C4 the emissivity profiles averaged over the set of field lines shown in Fig. 1. For each AIA channel, we further decompose the signal into contributions from “cold” ($T \ll 1$ MK) and “hot” ($T \gtrsim 1$ MK) plasma. In all channels, emission from hot plasma is either negligible or confined to the jet periphery, whereas the cold components exhibit a sharp peak at the nanojet core, indicating that the observed emission is primarily powered by dense ($\sim 10^{11}$ cm^{-3}) and cool ($\sim 10^{5}$ K) material.

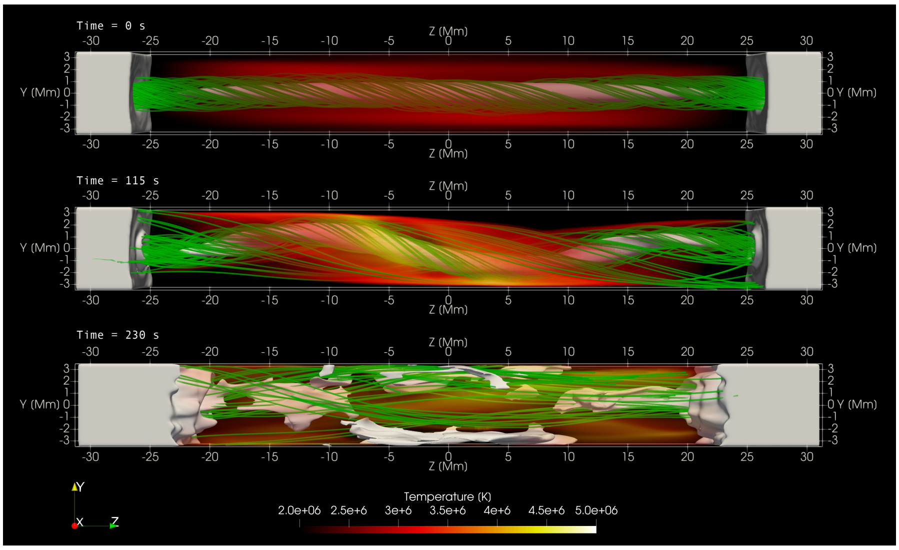

Fig. A1 3D rendering of the flux tube before (t = 0 s), during (t = 115 s) and after (t = 230 s) the kink instability. The volume rendering shows the high density filament regions ($\rho > 10^{10}\,\mathrm{cm}^{-3}$). Shades of red and yellow shows the coronal temperature distribution. Green magnetic field lines are traced from the left and right footpoints.

The plane-of-sky nanojet speed, as inferred from its EUV emission, was estimated using time–distance maps shown in Fig. C5. These were constructed by sampling the emission within the region bounded by the dashed lines in Fig. 3 and, for each snapshot, averaging along the vertical direction. This procedure traces the nanojet trajectory in the t–x plane. From the slope of this trajectory, we infer a projected in-plane velocity of $\approx 75\,\mathrm{km\,s^{-1}}$.

The nanojet emission measure in Fig. C6 was inferred from the synthetic maps in the six optically thin SDO/AIA EUV channels (94, 131, 171, 193, 211 and 335 Å). We applied a regularized inversion method [60] to recover the DEM from the multi-wavelength synthetic observations over the temperature range $\log_{10} T\,[\mathrm{K}] = 5.6$–$7.2$. We then compared the inverted EM to the "ground-truth" EM computed directly from the simulation data cube. The two distributions agree reasonably well at low temperatures (upper row in Fig. C6 and Fig. 4), but the inversion does not accurately reproduce the hot component (lower row). In particular, it produces an artificial excess in the $\log_{10} T\,[\mathrm{K}] = 6.4$–$6.6$ bin. Because several AIA temperature response functions are multi-peaked, this bias likely reflects a misattribution of emission in nominally high-temperature channels (e.g. 335 Å) to genuinely hot plasma, when it can instead be produced by dense, cooler material.

The EM-weighted temperature in Fig. C7 is computed from the synthetic (ground truth, left panel) and inverted (middle panel) emission measures shown in Figs. 4 and C6. In the synthetic data, the nanojet contains a cold, narrow core at $\lesssim 0.5\,\mathrm{MK}$,

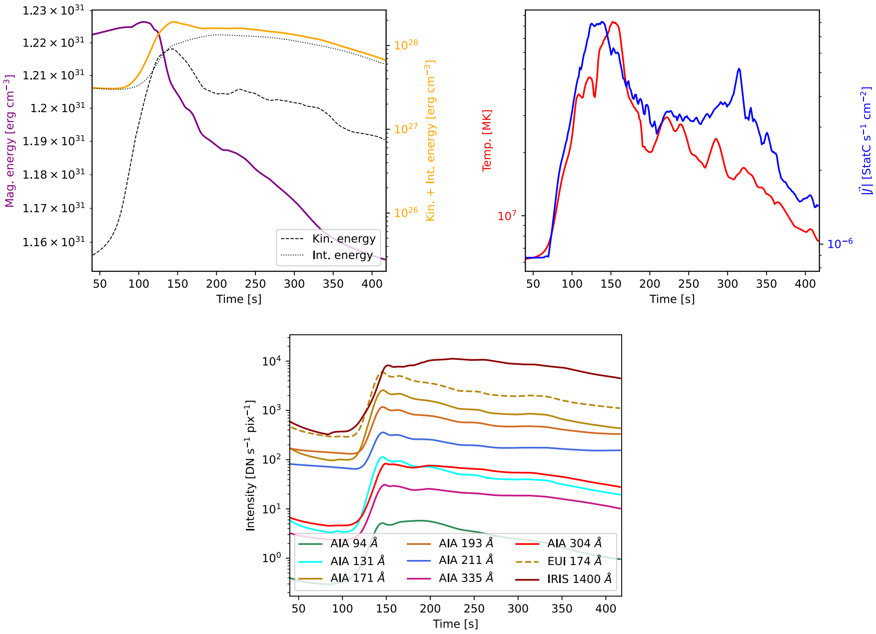

Fig. A2 Evolution of the total magnetic, kinetic, and internal energy (upper left), maximum temperature and current density (upper right), and averaged intensities (bottom) during the kink instability and later.

surrounded by an envelope in which the temperature transitions from sub- to multi-MK values. In the inverted temperature maps, the nanojet temperature is generally overestimated, typically lying in the 1–2 MK range, with little evidence for sub-MK plasma. The right panel of Fig. C7 shows the synthetic and inverted DEMs sampled at a representative nanojet location (marked by an "×"). The overplotted AIA 335 Å temperature response indicates that the spurious excess at $\sim 3\,$MK ($\log_{10}$ [K] ~ 6.5) arises from an overweighting of emission around the 335 Å response peak.

Figure C8 focuses on the latest stages of the nanojet evolution. The initial dense and cold jet-like structure (left) rapidly detaches from the plasma condensation on the left (mid), with the head of the jet being transported by the moving field line. After 10 s, it finally turns into a plasmoid (right), as its jet-like structure fades and it transitions into a clump-like morphology. It is still bright in the 174 Å channel of EUI and slightly visible also with IRIS SJI at 1400 Å. The plasmoid dissolves completely after a few tens of seconds.

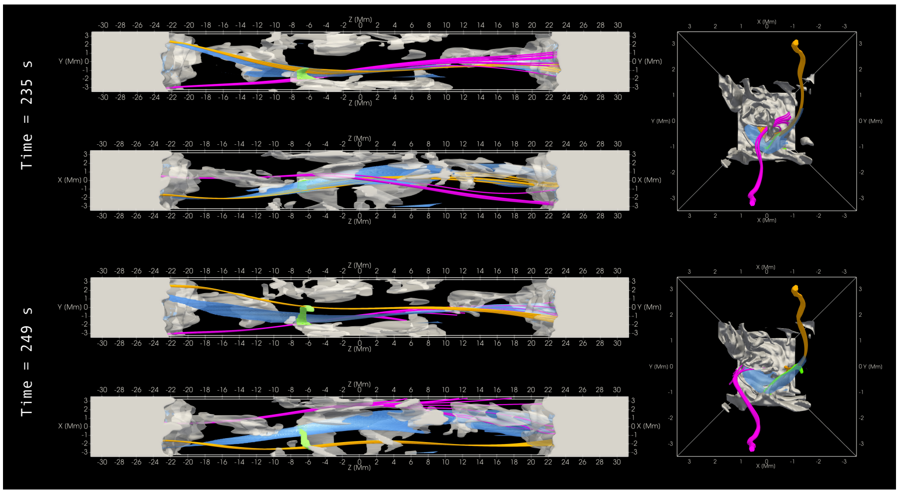

Fig. B3 3D rendering of the reconnection dynamics at the same times as in Fig. 1. For each snapshot time the three different orientations are shown. The white volume rendering shows the high density regions ($\rho > 10^{10}\,\mathrm{cm}^{-3}$). The nanojet plasma is emphasized by the green colour. Two reconnecting bundles of field lines are shown (magenta and orange), together with the current sheet (blue). A supplementary video is available.

Appendix D Spectroscopy with MUSE

We forward-modelled the MUSE observables, namely the intensity of the three main lines (Fe IX at 171 Å, Fe XV at 284 Å, and Fe XIX at 108 Å), along with their respective Doppler shift and non-thermal broadening maps. The nanojet is visible only in the channel at 171 Å, which is sensitive to lower temperatures ($\lesssim 1\,\mathrm{Mm}$). On the plane of the sky, as shown in Fig. C5, the jet plasma travels at a speed of $\sim 70\,\mathrm{km\,s^{-1}}$, which can be compared with the velocity of the moving field lines in Fig. 1. This latter velocity is estimated from the trajectory of the line in the time-distance plot of Fig. D10 (left panel) and is set at about $\sim 140\,\mathrm{km\,s^{-1}}$. The head of the jet is red-shifted as it moves away from the observer. Along the LoS, the maximum plasma velocity registered by the Doppler map is $\sim 200\,\mathrm{km\,s^{-1}}$, which is comparable with the projection of the field line velocity ($\sim 250\,\mathrm{km\,s^{-1}}$, Fig. D10, mid panel) but still smaller, as the partially diffusive plasma allows some slippage between the magnetic field and the plasma. A modest increase in the non-thermal line broadening is also registered (third panel on the right of Fig. D9, right panel in Fig. D10). The other two MUSE lines (Fe XV at 284 Å and Fe XIX at 108 Å) do not show clear evidence of a feature that resembles the nanojet, as they are sensitive to higher temperatures (2.5 MK and 10 MK, respectively). However, two long, blue- and red-shifted strands appear in the velocity maps of both channels, at the location of the reconnected field lines, linking the cold nanojet (bright at 171 Å) with a hot reconnection outflow. Similarly, the non-thermal line broadening becomes strong along the reconnected magnetic field.

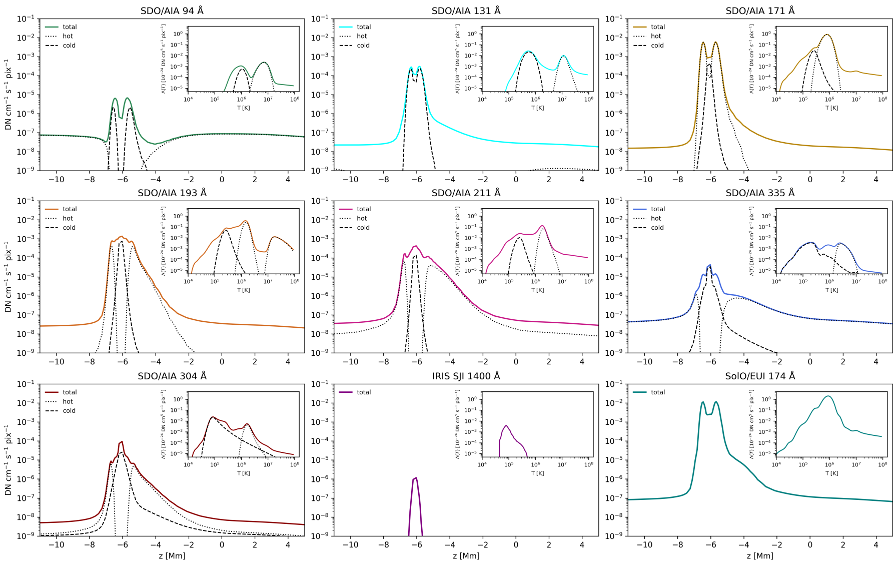

Fig. C4 Averaged emissivity in the SDO/AIA, SolO/EUI, and IRIS channels of Fig. 3, along the field lines in Fig. 1, at time $t = 249\,\mathrm{s}$. Total emission (solid lines), hot and cold contribution (dotted and dashed, respectively) are shown. The instrument response function for each channel is shown in the corresponding inset.

Appendix E Results for nanojet 2

A second nanojet was detected from time $t \sim 275\,\mathrm{s}$ at $z \sim 7\,\mathrm{Mm}$. In the synthetic EUV images, it propagates for about 30 s, reaching a maximum length of $\sim 2\,\mathrm{Mm}$ and an in-plane velocity of $\sim 75\,\mathrm{km\,s^{-1}}$. As for the first nanojet, it consists of cold and dense TR plasma enveloped by increasingly hot coronal plasma. The DEM inversion shows an excess of plasma in the $\log_{10}$ [K]:6.4-6.5 temperature bin, as the brightness in the AIA 335 Å channel is incorrectly attributed to plasma at $\sim 3\,\mathrm{MK}$, leading to an overestimate of the nanojet temperature.

From synthetic MUSE data, we can gather information about the nanojet LOS velocity and the dynamics of the hot coronal plasma around it. The head of the nanojet, visible in the 171 Å channel, is blue-shifted at $\sim 50\,\mathrm{km\,s^{-1}}$, giving a total velocity of $\sim 90\,\mathrm{km\,s^{-1}}$. The nanojet is no longer visible in the hot MUSE channels, but they help to pinpoint the region where reconnection takes place. Specifically, a narrow strand is bright in the 108 Å channel and shows strong red-shifts and non-thermal broadening. It is located at the border of the cold plasma cloud from which the nanojet originates, suggesting that reconnection occurs nearby, rapidly heats up the plasma around it, and accelerates a reconnection outflow from which the nanojet originates.

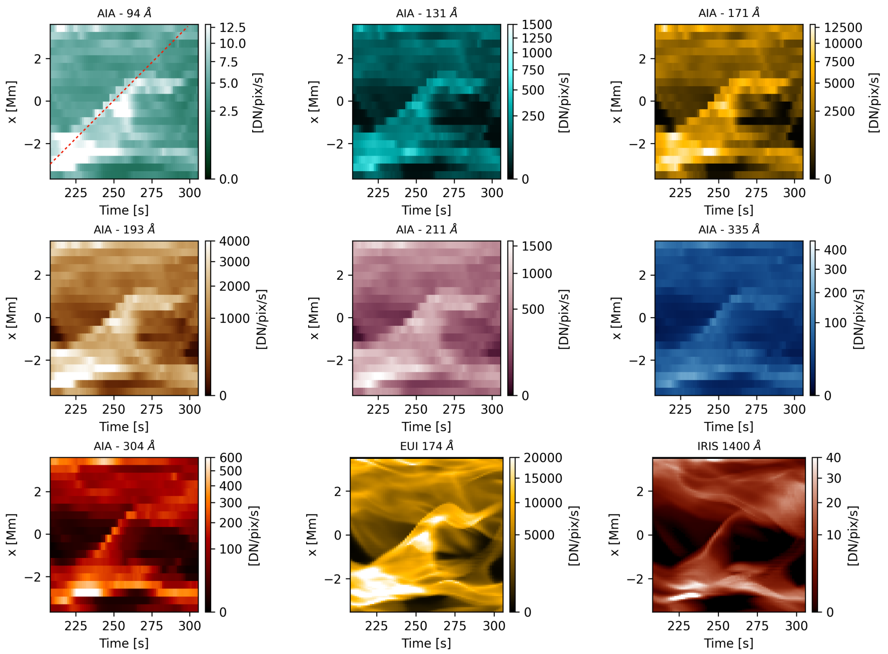

Fig. C5 Time distance maps of nanojet EUV emission along the white lines of figure 3. The nanojet trajectory between $t = 230\,\mathrm{s}$, and $t = 260\,\mathrm{s}$ (dashed red line in the first panel) has slope of $70\,\mathrm{km/s}$.

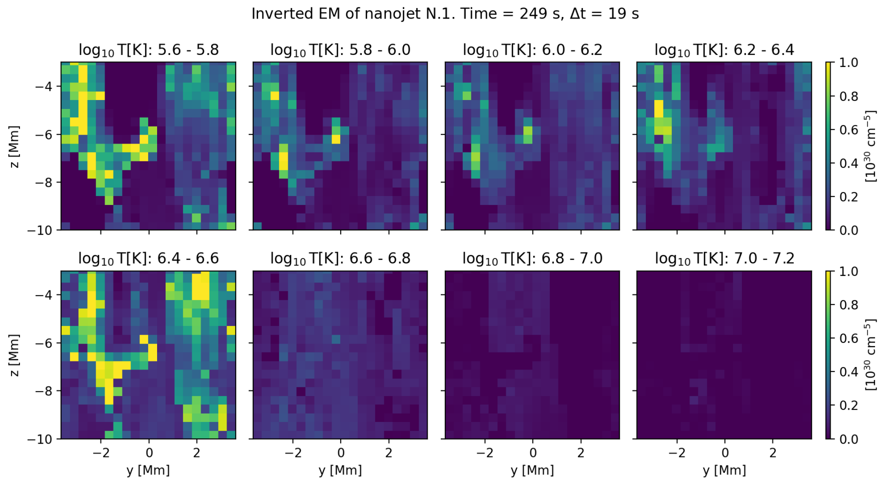

Fig. C6 Nanojet plasma emission measure (EM), as inverted from the AIA synthetic emission, across 8 logarithmically spaced temperature bins $\log_{10} T\,[\mathrm{K}] = 5.6$ to $\log_{10} T\,[\mathrm{K}] = 7.2$. A supplementary video is available.

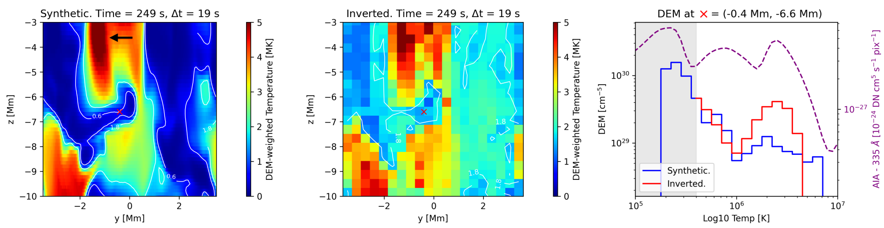

Fig. C7 Synthetic (first map) versus inverted (second map) DEM-weighted temperature of the region in Figs. C6 and 4. Isocontours at $T = 0.6\,\mathrm{MK}$ and $1.8\,\mathrm{MK}$ are plotted in white. The black arrow pinpoints very hot plasma in the vicinity of the reconnection point. Third panel: DEM distributions from the two methods at $\times$ =(-0.4 Mm, -6.6 Mm), the grey area is outside the DEM-inversion temperature range. The AIA response function at 335 Å is overplotted (purple dashed line).

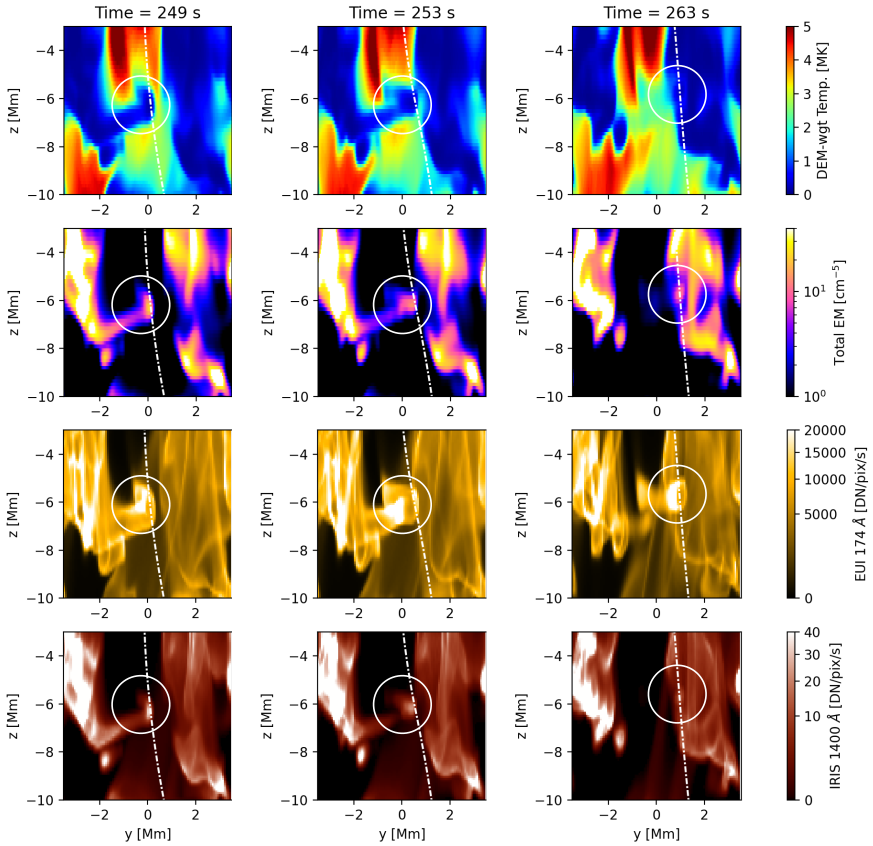

Fig. C8 Latest stages of the nanojet evolution. The panels show a zoom in of the temperature (first row), EM (second), and intensity in the EUI 174 Å (third) and IRIS 1400 Å (fourth) channels, at three different times towards the end of the nanojet journey. A (dot-dashed) field line is over-plotted. the moving plasmoid is circled.

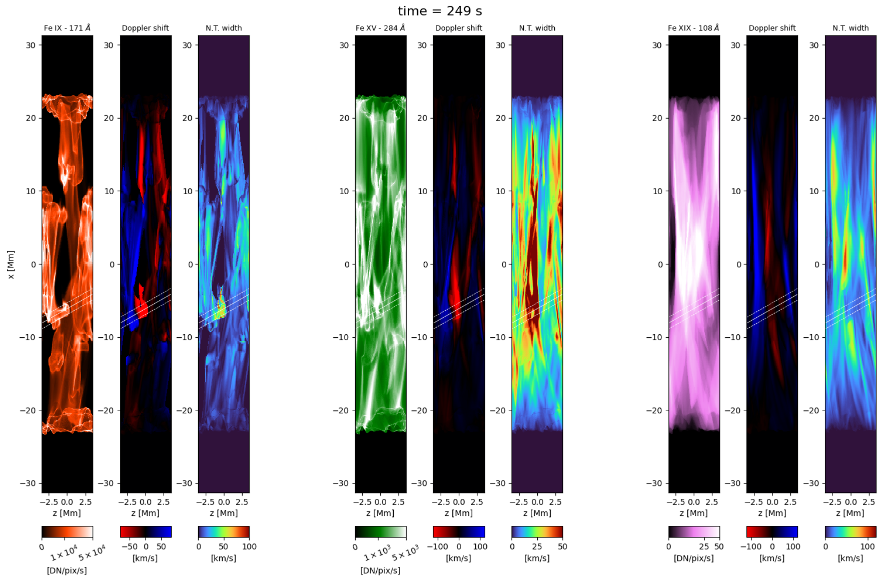

Fig. D9 Synthesis of the EUV emission, Doppler shifts and non-thermal line width across the three MUSE lines at 171 Å (Fe IX), 284 Å (Fe XV), and 108 Å (Fe XIX). A solid white line aligns with the nanojet direction of propagation, dashed lines visually estimate the width. A supplementary video is available.

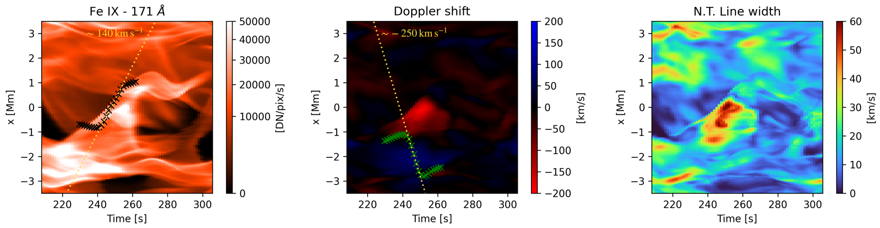

Fig. D10 Time distance maps of nanojet EUV emission, Doppler shifts, and non-thermal line width in the 171 Å channel of MUSE along the white lines of figure D9. The "×" markers in the first (second) panel shows the averaged x (y) coordinate of field lines bundle shown in Fig. 1 across the time. The v_x (v_y) velocity component is estimated from the slope of dotted yellow line.